



# A continuum damage mechanics approach coupled with an improved pit evolution model for the corrosion fatigue of aluminum alloy



Ping Hu<sup>a</sup>, Qingchun Meng<sup>a,b</sup>, Weiping Hu<sup>b,\*</sup>, Fei Shen<sup>c</sup>, Zhixin Zhan<sup>b</sup>, Linlin Sun<sup>b</sup>

<sup>a</sup> School of Astronautics, Beihang University, Beijing 100191, China

<sup>b</sup> Institute of Solid Mechanics, School of Aeronautics Science and Engineering, Beihang University, Beijing 100191, China

<sup>c</sup> School of Mechanical and Aerospace Engineering, Nanyang Technological University, Singapore 639798, Singapore

## ARTICLE INFO

### Article history:

Received 3 May 2016

Received in revised form

18 September 2016

Accepted 13 October 2016

Available online 14 October 2016

### Keywords:

A. Aluminum

B. Modelling studies

C. Pitting corrosion

D. Corrosion fatigue

## ABSTRACT

In this study, a continuum damage mechanics approach coupled with an improved pit evolution model was proposed to predict the corrosion fatigue life of aluminum alloy. The coupled elasto-plastic damage constitutive equations and elastic–plastic damage evolution models were adopted to evaluate the fatigue damage. Pit growth was modeled with considering the effects of multiaxial stresses and fatigue damage. Numerical simulations were then implemented using the ABAQUS, and the results were compared with the experimental data. In addition, the interaction between corrosion and fatigue damage was presented, and the effects of the stress level and loading frequency were examined.

© 2016 Elsevier Ltd. All rights reserved.

## 1. Introduction

Aluminum alloys are widely used in the aviation and aerospace industries owing to their superior mechanical performance and lower density compared with other metals. The fatigue performance of an aluminum alloy is one of its most important properties in practical applications. Many researchers have reported that the fatigue life of an aluminum alloy is highly influenced by environmental factors in addition to the cyclic loading which is usually given more attention. Corrosion pits may be generated and grow on the surfaces of materials in harsh environments [1,2]. The physical and chemical heterogeneities on the surface, such as inclusions, flaws, and dislocations, play important roles in the formation of corrosion pits [3,4–8]. Based on the knowledge that the fatigue life of metals can be significantly reduced by the presence of corrosion pits [5,9,10], the mechanism by which pitting corrosion influences the fatigue crack initiation has been widely studied since the 1920s. From a qualitative point of view, the effect of pits is mainly attributed to changes in the material surface morphology, which gives rise to stress concentrations. Thus, fatigue cracks tend to nucleate around corrosion pits [11,12]. However, although quan-

titative methods are more important than qualitative methods in engineering applications, it is difficult to build a satisfactory quantitative model owing to the complexity of the corrosion fatigue process. This process includes the stages of pit initiation, pit growth, crack initiation, and crack propagation. In most cases, pit growth and crack initiation take up the majority of the corrosion fatigue life of the components [13]. Thus, predicting the pit-to-crack transition life is the most critical issue in corrosion fatigue analysis. This is the focus of this study.

Typically, analysis of the pit-to-crack transition life involves a pit evolution model and a crack initiation model. For the pit evolution model, many researchers, such as Kondo [14] and Harlow et al. [15], have assumed that the growth of the pit follows Faraday's law, which assumes that the volumetric growth rate remains constant during corrosion fatigue. Furthermore, as the volume of a pit is closely related to its shape, various assumptions concerning pit shape have been examined [16,17–22]. Ghali et al. [16] and Codaro et al. [17] concluded from experimental observations that the shapes of pits are influenced by the distribution of corrosion potential around the pits. After observing the evolution of corrosive pits of an aluminum alloy under water, Godard et al. [18] concluded that pits grow at the same rate in any direction and proposed an assumed hemispherical pit shape. Harlow et al. [19] and Chen et al. [20] proposed an assumed semi-ellipsoid pit shape based on experimental observations. However, Harlow et al. [19] assumed that the shape factor, denoted by  $c/a$  (where  $c$  represents the diameter

\* Corresponding author at: Room D604, New Main Building, 37th Xueyuan Road, Beihang University, Beijing, 100191, China.

E-mail address: [huweiping@buaa.edu.cn](mailto:huweiping@buaa.edu.cn) (W. Hu).

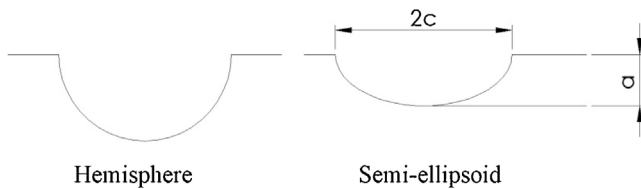


Fig. 1. 2-D profiles of pit shapes for hemispherical and semi-ellipsoid pit shape assumptions.

of the pit surface and  $a$  represents the depth of pit), is constant, whereas Chen et al. [20] assumed that the shape factor changes over time. Fig. 1 illustrates the two-dimensional (2-D) profiles of pit shapes corresponding to the hemispherical and semi-ellipsoid shape assumptions. Burns and Kim et al. [21,22] investigated the corrosion morphology of 7075-T6511 aluminum alloy by using the crack surface marker-band analysis. They found that at the initial stage, the surface damage induced by a corrosive environment occurred at the constituent particles or along grain boundaries. This surface damage is characterized by isolated pits with hemispherical shapes, and these pits tend to coalesce to create wider pits with high  $c/a$  ratios as the exposure time increases.

With respect to the crack initiation, two approaches to modeling the pit-to-crack transition, based on fracture mechanics [5,19,20,23,24] and continuum damage mechanics (CDM) [25], have been widely studied. In the fracture mechanics-based approach, pits are considered to be equivalent to surface cracks, and two models have been proposed—a critical pit size model and a model for the competition between the pit growth rate and the crack growth rate. The critical pit size model seeks to determine the critical size of the corrosion pit corresponding to crack initiation by evaluating the local mechanical condition. Hoepfner [26] and Muller [27] suggested that a crack nucleates from a pit when the stress intensity factor reaches the threshold of the fatigue crack growth. Chen et al. [20] calculated the critical stress intensity factor based on the fractographic shape and size. In contrast, Kondo [14] proposed a competition model for the relation between the pit growth rate and crack growth rate. He proposed a criterion for crack initiation that depends on whether the crack growth rate exceeds the pit growth rate. In Kondo's model, the crack growth rate is formulated using the fracture mechanics method, while the pit growth rate is modeled via Faraday's law. Fracture mechanics-based models, which provide a theoretical framework for crack nucleation analysis using several fracture mechanics parameters, are convenient for use in practical applications and predict corrosion fatigue life fairly well. However, the complex interaction between the fatigue and pit evolution cannot be described explicitly. In addition to fracture mechanics, continuum damage mechanics plays an important role in addressing this issue. In CDM-based approaches, pits are considered to be notches rather than surface cracks. Sankaran et al. [10] concluded that the effects of pitting corrosion on the fatigue life can be related to the effects of the equivalent stress concentration factor. Furthermore, Amiri et al. [25] presented a CDM model for the pit-to-crack transition in which the pit is regarded as a notch and the growth of pit is assumed to follow Faraday's law. Amiri et al. [25] adopted the fatigue damage evolution model proposed by Xiao et al. [28] for cases of high-cycle fatigue and validated the applicability of that simple CDM model. However, the plastic deformation in the vicinity of the pit was not considered in that research. The authors [29] of the present study have previously proposed a CDM model to study the pre-corrosion and corrosion fatigue of aluminum alloys, but changes in the corrosive morphology during the corrosion fatigue process and plastic fatigue damage were not considered in that research.

Another important issue in pit evolution is the development of a numerical method for simulating the metal dissolution that occurs during the corrosion process. It is difficult to simulate the evolution of the pit morphology because the movement of the corrosion interface can be very rapid and therefore requires an extensive re-meshing during finite element (FE) analysis. To address this issue, an advanced FE technique, the arbitrary Lagrangian–Eulerian (ALE) method, was employed in a recent research [30]. Kota et al. [31] presented the numerical modeling of a stable pit growth in his work to study the influence of the microstructure on the pit shape. Sun et al. [32] proposed an ALE model to simulate the time-dependent evolution of crevice corrosion. The deformation of the crevice geometry was implemented using the ALE method. In this study, an ABAQUS user subroutine called UMESHMOTION was used to set up an ALE model for simulation of pitting.

This study presented a CDM approach combined with an improved pit evolution model for use in investigating the pit-to-crack transition for aluminum alloy. The coupled elasto-plastic damage constitutive model was adopted to calculate the stresses and strains of a specimen with pits. Fatigue damage was calculated using two evolution models to account for the elastic and plastic fatigue damages. The pit evolution model was improved by considering the effects of the fatigue damage and cyclic multi-axial stresses. Numerical simulations were implemented by using ABAQUS. The UMAT user subroutine was used to implement the coupled elasto-plastic damage constitutive model and two fatigue damage evolution models, and the UMESHMOTION user subroutine was used to model the growth of the pit. The improved pit evolution model was validated by comparing the numerical results with experimental data. Following that the pit evolution and fatigue damage were studied, and the interaction between them was investigated. The process of material degradation resulting from the coupled effects of corrosion and fatigue was clarified. In addition, the effects of pit morphology, stress level, and loading frequency on the corrosion fatigue life were examined.

## 2. Theoretical model

The theoretical model used in this study for the analysis of corrosion fatigue consisted of three components: a coupled elasto-plastic damage constitutive model, a fatigue damage evolution model, and an improved pit evolution model. Each of these three models is described below.

### 2.1. Coupled elasto-plastic damage constitutive model

For the case of small deformations, the elastic constitutive model of the undamaged material can be written as follows [33]:

$$\varepsilon_{ij}^e = \frac{1+\nu}{E} \sigma_{ij} - \frac{\nu}{E} \sigma_{kk} \delta_{ij} \quad (1)$$

where  $E$  and  $\nu$  are the Young's modulus and Poisson's ratio of the undamaged material, respectively;  $\sigma_{ij}$  is the Cauchy stress tensor, and  $\varepsilon_{ij}^e$  is the elastic strain tensor.

In a mechanical sense, damage in a solid materials is the creation and growth of microvoids or microcracks, which are discontinuities in a medium considered as continuous at a larger scale [34]. To estimate the progressive deterioration of the material due to fatigue loading, the following damage variable, which is a state variable in the thermodynamic context, is introduced [34]:

$$D = \frac{\delta S_D}{\delta S} \quad (2)$$

where  $\delta S$  is the area of a section of the representative volume element, in which all properties are represented by homogeneous variables and  $\delta S_D$  is the total area of microcracks and microvoids.

In the context described below, the damage variable,  $D$ , is referred to simply as damage. Although fatigue damage is anisotropic even for initially isotropic materials, it is considerably more difficult to adopt the anisotropic damage models [35,36,37] owing to the complexity in parameter calibration and fatigue damage calculation involved. Thus, the isotropic assumption with acceptable results for crack initiation is still used. The stress acting on the resisting area is referred to as the effective stress. The effective stress is defined as follows [34]:

$$\tilde{\sigma} = \frac{\sigma}{1-D} \quad (3)$$

where  $\tilde{\sigma}$  is the effective stress.

Based on the hypothesis of strain equivalence and the isotropic assumption [38], we can derive the coupled elastic damage constitutive equation as follows:

$$\varepsilon_{ij}^e = \frac{1+\nu}{E} \frac{\sigma_{ij}}{1-D} - \frac{\nu}{E} \frac{\sigma_{kk} \delta_{ij}}{1-D} \quad (4)$$

Owing to the corrosive environment that leads to the formation of corrosion pits and results in stress concentration, the local plastic deformation may occur in the vicinity of corrosion pits when the fatigue stress level is high. The Chaboche plasticity model [39,40] was adopted in this study because of its widespread applicability. In the case of small deformations, the total strain is composed of two components: elastic strain and plastic strain:

$$\varepsilon_{ij} = \varepsilon_{ij}^e + \varepsilon_{ij}^p \quad (5)$$

The yield function and the plastic flow with damage can be written as follows:

$$F = \left( \frac{\sigma_{ij}}{1-D} - \alpha_{ij} \right)_{\text{eq}} - Q \quad (6)$$

$$\dot{\varepsilon}_{ij}^p = \dot{\lambda} \frac{\partial F}{\partial \sigma_{ij}} = \frac{3}{2} \frac{\dot{\lambda}}{1-D} \left( \frac{\sigma_{ij}}{1-D} - \alpha_{ij} \right)_{\text{dev}} \quad (7)$$

$$\dot{p} = \sqrt{\frac{2}{3} \dot{\varepsilon}_{ij}^p \dot{\varepsilon}_{ij}^p} = \frac{\dot{\lambda}}{1-D} \quad (8)$$

where the subscripts “dev” and “eq” denote the deviatoric component of stress and the von Mises equivalent stress, respectively;  $Q$  is the size of the yield surface,  $\alpha_{ij}$  is the back stress tensor,  $\dot{\lambda}$  is the plastic multiplier, and  $\dot{p}$  is the accumulated plastic strain rate.

Isotropic hardening was not considered in this study. The size of the yield surface,  $Q$ , was assumed to remain constant. That means the value of  $Q$  in Eq. (6) equals  $\sigma_y$ , the initial yield stress.

The kinematic hardening law with damage is written as follows:

$$\alpha_{ij} = \sum_{k=1}^n \alpha_{ij}^{(k)} \quad (9)$$

$$\dot{\alpha}_{ij}^{(k)} = (1-D) \left( \frac{2}{3} C_k \dot{\varepsilon}_{ij}^p - \gamma_k \alpha_{ij}^{(k)} \dot{p} \right) \quad (10)$$

where  $C_k$  and  $\gamma_k$  are material constants whose values are calibrated using experimental data and  $n$  is the number of the back stress components. Three sets of back stresses were employed in this study.

It should be noted that a coupled theory of damage mechanics and finite strain elasto-plasticity should be adopted in the case of finite strain plasticity [41,42].

## 2.2. Fatigue damage model

Two damage evolution models, a stress-based model, and a plastic strain-based model are needed for the analysis of corrosion

fatigue. In addition to elastic damage, plastic damage may exist in the vicinity of corrosion pits as a result of stress concentration.

### 2.2.1. Stress-based damage evolution model

Lemaitre and Chaboche et al. [33] proposed the following uniaxial fatigue damage model suitable for describing high-cycle fatigue behavior:

$$\frac{dD_e}{dN} = [1 - (1-D)^{\beta+1}]^\alpha \cdot \left[ \frac{\sigma_a}{M_0(1-b_2\sigma_m)(1-D)} \right]^\beta \quad (11)$$

where  $D_e$  is the elastic fatigue damage;  $N$  is the number of cycles;  $\beta$ ,  $M_0$ , and  $b_2$  are material constants; and  $\sigma_a$  and  $\sigma_m$  are the amplitude of stress and the average stress, respectively. The parameter,  $\alpha$ , is expressed as follows:

$$\alpha = 1 - a \left\langle \frac{\sigma_a - \sigma_{10}(1-b_1\sigma_m)}{\sigma_u - \sigma_{\max}} \right\rangle \quad (12)$$

where  $a$  and  $b_1$  are material constants,  $\sigma_u$  is the ultimate tensile stress,  $\sigma_{10}$  is the fatigue limit at the fully reversed loading condition, and  $\sigma_{\max}$  and  $\sigma_m$  are the maximum stress and the mean stress of cyclic loading, respectively.

For the case of multiaxial stress, Chaudonneret [43] proposed the following multiaxial fatigue damage model, based on the Chaboche model [33]:

$$\frac{dD_e}{dN} = [1 - (1-D)^{\beta+1}]^\alpha \cdot \left[ \frac{A_{II}}{M_0(1-3b_2\sigma_{H,\text{mean}})(1-D)} \right]^\beta \quad (13)$$

$$\alpha = 1 - a \left\langle \frac{A_{II} - \sigma_{10}(1-3b_1\sigma_{H,\text{mean}})}{\sigma_u - \sigma_{\text{eq,max}}} \right\rangle \quad (14)$$

where  $\sigma_{\text{eq,max}}$  is the maximum equivalent stress over a loading cycle,  $A_{II}$  is the amplitude of the octahedral shear stress, and  $\sigma_{H,\text{mean}}$  is the mean value of the hydrostatic stress.  $A_{II}$  and  $\sigma_{H,\text{mean}}$  can be expressed as follows:

$$A_{II} = \frac{1}{2} \left[ \frac{3}{2} (S_{ij,\text{max}} - S_{ij,\text{min}})^2 \right]^{1/2} \quad (15)$$

$$\sigma_{H,\text{mean}} = \frac{1}{6} [\max(\text{tr}(\sigma)) + \min(\text{tr}(\sigma))] \quad (16)$$

It should be noted that the stress-based damage evolution model was used in this study to calculate the evolution of the damage caused by elastic deformation.

### 2.2.2. Plastic strain-based damage evolution model

Lemaitre proposed a plastic strain-based damage evolution model for ductile failure [34]. This model can be extended to the calculation of the incremental fatigue damage caused by the plastic strain. The damage accumulation over each cycle is calculated as follows:

$$\frac{dD_p}{dN} = \left[ \frac{(\sigma_{\max}^*)^2}{2ES(1-D)^2} \right]^m \Delta p \quad (17)$$

where  $D_p$  is the plastic damage, and  $\sigma_{\max}^*$  is the maximum value of the damage equivalent stress [44] over a loading cycle, and  $S$  and  $m$  are material constants whose values are calibrated using experimental data.

## 2.3. Improved pit evolution model

### 2.3.1. Pit evolution model

Many researchers have studied the nucleation and growth of corrosion pits on stainless steel [45–46,47] and aluminum alloys [48]. As Kang et al. [49] explained, in the case of aluminum alloys,

**Table 1**

Calibrated values of parameters of the coupled elasto-plastic damage constitutive model for 2024-T3.

$E$ (MPa)	$\nu$	$\sigma_y$ (MPa)	$C_1$ (MPa)	$C_2$ (MPa)	$C_3$ (MPa)	$\gamma_1$	$\gamma_2$	$\gamma_3$
73,000	0.33	289	2169.7	7471.9	65,761	11.74	90.05	555.09

pitting corrosion usually originates in the region between S-phase particles and the surrounding aluminum matrix. Aluminum alloys containing intermetallic compounds have a potential for corrosion by inducing anodic dissolution between the particles and the aluminum matrix.

Pitting corrosion can be characterized by two major types of events, i.e., early metastable growth and subsequent stable growth [45,50]. The growth rate of metastable pits depends on the microstructure of the alloy and is thus a distributed value [50]. Metastable pits form and grow in small size and repassivate in a few seconds. The transition from metastable pits to stable growth is stochastic in nature [50]. The boundary between metastable pits and stable pit growth is the critical pitting potential. Metastable pits initiate and grow below the critical pitting potential, while the stable pit growth occurs above the critical pitting potential [51]. Williams et al. [52] elaborated a criterion for the pit stabilization on steel based on the value of  $I_{\text{pit}}/r_{\text{pit}}$ . A stable growth occurs when  $I_{\text{pit}}/r_{\text{pit}}$  exceeds  $4 \times 10^{-2}$  A/cm.  $I_{\text{pit}}$  is the current within the pit, and  $r_{\text{pit}}$  is the radius of the pit. This criterion has also been applied to aluminum alloys. In this study, stable pit growth was considered a critical issue.

The main task of illustrating the characteristics of stable growth is the establishment of the kinetics of pit growth. Many studies on pit growth have been performed using different types of experiments. Pitting is induced by particles, and the pitting current is determined by the cathodic current density. The galvanic coupling of constituent particles and the alloy matrix promotes the dissolution of the matrix. Harlow and Wei et al. [15,53] proposed a model describing pits initiating from surface particles as a result of galvanic corrosion in the matrix. With continuous exposure to the corrosive environment, particles on the surface induce a galvanic current and promote the growth of pits. In this study, we sought to describe stable pit growth by using a simplified model for analyzing the interaction and combined impact of pitting corrosion and fatigue damage.

Pits that form on the surfaces of materials due to corrosion will continue to grow in a corrosive environment. Pit growth is directly related to the corrosion time and external loading. Faraday's law is commonly used in the pit evolution model. This law assumes that the volumetric growth rate of a pit is constant until a critical depth is reached. There may be several pits on the surface of a specimen. However, only one of them is the most critical. Therefore, the single dominant flaw approach [25,54] was adopted in this study, i.e., only one pit, which is assumed to grow into the critical depth and nucleate fatigue crack, was modeled. The equation for the evolution of the critical pit is expressed as follows [14]:

$$\frac{dV}{dt} = \frac{MI_p}{\rho nF} = \frac{MI_{p0}}{\rho nF} \exp\left[-\frac{\Delta H}{RT}\right] \quad (18)$$

where  $V$  is the pit volume,  $M$  is the relative atomic mass of the material,  $I_p$  is the pitting current,  $I_{p0}$  is the pre-exponential term in the Arrhenius relationship [25] that influences the growth rate of the pit,  $\rho$  is the material density,  $n$  is the atomic valence,  $F$  is Faraday's constant,  $\Delta H$  is the activation enthalpy of pit corrosion,  $R$  is the universal gas constant, and  $T$  is the absolute temperature.

Experimental observation [19–22] indicate that the shape of a corrosion pit can be assumed to be semi-ellipsoid [25,55], with an aspect ratio  $\lambda = c/a$ , and that  $\lambda$  remains constant during the entire

corrosion fatigue process. Therefore, the right term of Eq. (18) can be written as follows:

$$\frac{dV}{dt} = 2\pi\lambda^2 a^2 \frac{da}{dt} \quad (19)$$

where  $a$  is the depth of the corrosion pit, and  $\lambda = c/a$  is the elliptical ratio. Using Eq. (19) and integrating Eq. (18) with respect to time from 0 to  $t$ , we can obtain the following expression for the pit depth at any time:

$$a^3 = \frac{3MI_{p0}}{2\pi\lambda^2 \rho nF} \exp\left[-\frac{\Delta H}{RT}\right] t + a_0^3 \quad (20)$$

where  $a_0$  is the initial depth of the pit, which was assumed to be zero in this study.

However, the model described by Eq. (20) does not consider the effect of cyclic stress on the pit growth rate. Studies by Ishihara et al. [23], Kondo [14], and Amiri et al. [25] have all shown that cyclic stress may increase the pit growth rate. Ishihara et al. [23] proposed the following exponential relationship between the pit growth rate and the cyclic stress amplitude:

$$\frac{dV}{dt} = \frac{MI_{p0}}{\rho nF} \exp\left[-\frac{\Delta H}{RT}\right] A^{\sigma_a} \quad (21)$$

where  $\sigma_a$  is the amplitude of the cyclic load and  $A$  is a constant whose value was calibrated using experimental data. An empirical value of  $A = 1.014$  is adopted in this study in accordance with the recommendation of Ishihara et al. [23]. This empirical value was subsequently validated by comparison of calculated results with experimental data.

### 2.3.2. Improved pit evolution model

In this study, the amplitude of the cyclic load,  $\sigma_a$ , in Eq. (21) was replaced with the amplitude of the octahedral shear stress,  $A_{II}$ . The reason for this modification was that, in the original model,  $\sigma_a$  represents the remote stress amplitude, which remains constant during the cyclic loading. From a physical point of view, the pit growth rate is closely related to the local stress state around the pit. Thus,  $A_{II}$  obtained from the bottom of the pit was substituted for  $\sigma_a$  as the driving force facilitating the pit growth. This substitution is also convenient for describing the case of a multiaxial stress state, which is more common in practical situations.

$A_{II}$  is calculated according to the stress state of the element at the center of the pit. The value of  $A_{II}$  is influenced by both the morphology of the pit and the accumulated fatigue damage around the pit. Accordingly, the effects of multiaxial cyclic stresses and fatigue damage on the growth rate of the pit are involved in the pit evolution model.  $A_{II}$  is calculated as shown in Eq. (15). In a form similar to that of Eq. (20), the pit depth can be expressed as a function of the corrosion time  $t$  and the octahedral shear stress  $A_{II}$ :

$$a^3 = A^{A_{II}} \frac{3MI_{p0}}{2\pi\lambda^2 \rho nF} \exp\left[-\frac{\Delta H}{RT}\right] t + a_0^3 \quad (22)$$

## 3. Calibration of material parameters

Four sets of material parameters must be calibrated: one set in the coupled elasto-plastic damage constitutive model, two sets in the two types of fatigue damage models, and one set in the improved pit evolution model. The following is a brief introduction on the process of parameter calibration. The reader is referred to the literature [44,56,57] for more details.

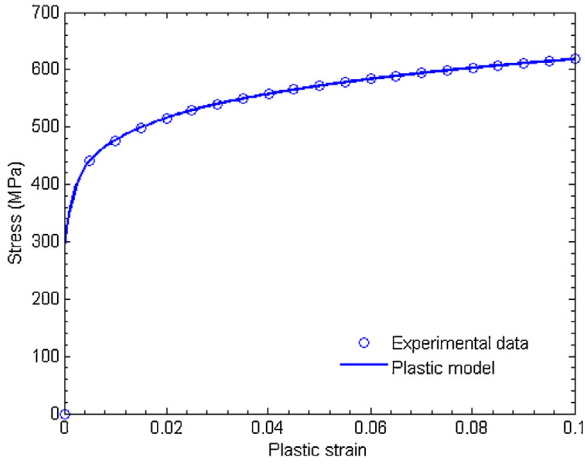


Fig. 2. Plastic model curve fitted to experimental data.

Aluminum alloy 2024-T3 was considered in this study. The maximum load is relatively small in the case of validation of the improved pit evolution model and the plastic deformation does not occur around the pit. Therefore, only the parameters in the stress-based fatigue damage model, elastic constitutive model, and improved pit evolution model need to be calibrated. However, for the case of corrosion fatigue, plastic deformation occurs around the pit. Thus, all four sets of parameters are adopted for the analysis. It should be noted that the material in the case of corrosion fatigue is aluminum alloy LY12CZ [58] (in China), which is actually equivalent to aluminum alloy 2024-T3 (in USA). Therefore, we regard LY12CZ and 2024-T3 as the same material, and all their parameters are considered to be the same.

### 3.1. Parameters in the coupled elasto-plastic damage constitutive model

Isotropic hardening is neglected in this study, and therefore, only  $C_k$  and  $\gamma_k$  in the kinematic hardening need to be calibrated. The plastic stress–strain relationship for the case of uniaxial loading can be written as follows:

$$\sigma = \sigma_y + \sum_{k=1}^n \frac{C_k}{\gamma_k} (1 - e^{-\gamma_k \varepsilon_p}) \quad (23)$$

The least square method was used to calibrate the three sets of parameters of  $C_k$  and  $\gamma_k$  by fitting experimental data to the uniaxial monotonic tension stress–strain curve.

The material parameters in the coupled elasto-plastic damage constitutive model were calibrated using the experimental data obtained from the literature [3]. The calibrated values are provided in Table 1. The fitted curve and the experimental data for uniaxial loading are shown in Fig. 2.

### 3.2. Parameters in the stress-based damage evolution model

The five parameters in the stress-based damage model that need to be calibrated are  $\beta$ ,  $M_0$ ,  $a$ ,  $b_1$ , and  $b_2$ , as shown in Eqs. (13) and (14). A closed form of the fatigue life expression for a smooth specimen undergoing constant amplitude cyclic loading can be obtained by integrating the elastic damage evolution equation in its uniaxial form. The integral form of Eq. (13) is as follows:

$$N_f = \frac{1}{1 + \beta} \frac{1}{aM_0^{-\beta}} \frac{\langle \sigma_u - \sigma_{\max} \rangle}{\langle \sigma_a - \sigma_{10} (1 - b_1 \sigma_m) \rangle} \left[ \frac{\sigma_a}{1 - b_2 \sigma_m} \right]^{-\beta} \quad (24)$$

Table 2

Calibrated material parameter values in the stress-based damage evolution model for 2024-T3.

$\beta$	$aM_0^{-\beta}$	$b_1$	$b_2$	$a$
1.3812	7.03E-9	0.0021	0.0031	0.75

Table 3

Calibrated material parameters of plastic strain-based damage evolution model for 2024-T3.

$S$ (MPa)	$m$
6.2925	2.4965

The values of the parameters,  $\beta$  and  $aM_0^{-\beta}$ , can then be determined by fitting Eq. (24) to experimental data from stress-controlled fatigue test conducted under fully reversed loading condition. The values of the parameters,  $b_1$  and  $b_2$ , can be obtained from fatigue experiments conducted at different mean stresses. The value of the parameter,  $a$ , can be determined by the method proposed by Zhang [44].

The values of the material parameters in the stress-based damage evolution model for 2024-T3 were calibrated using experimental data obtained from the literature [59]. The calibrated values are listed in Table 2.

### 3.3. Parameters in the plastic strain-based damage evolution model

Two parameters in the plastic strain-based damage evolution model,  $S$  and  $m$ , need to be calibrated. The closed form of the fatigue life expression can be obtained by integrating Eq. (17) in its uniaxial form, which is expressed as follows:

$$N_f = \frac{1}{2(2m + 1)} \Delta \varepsilon_p \left( \frac{2ES}{(\sigma_{\max})^2} \right)^m \quad (25)$$

where  $\sigma_{\max}$  can be expressed as a function of the  $\Delta \varepsilon_p$  as follows:

$$\sigma_{\max} = K' \left( \frac{\Delta \varepsilon_p}{2} \right)^{n'} \quad (26)$$

where  $K'$  and  $n'$  can be obtained by experiments. By substituting Eq. (25) to Eq. (26), we obtain the following expression:

$$N_f = \frac{1}{2(2m + 1)} \left( \frac{2^{1+2n'} ES}{(K')^2} \right) (\Delta \varepsilon_p)^{-(1+2mn')} \quad (27)$$

By comparing Eq. (27) with the Coffin–Manson equation shown as Eq. (28), the values of the parameter  $S$  and  $m$  can be obtained from the values of  $\varepsilon_f$ ,  $c$ ,  $K'$ , and  $n'$ .

$$\frac{\Delta \varepsilon_p}{2} = \varepsilon_f (2N_f)^c \quad (28)$$

where  $\varepsilon_f$  is the fatigue ductility coefficient and  $c$  is the fatigue ductility exponent.

The material parameters in the stress-based damage evolution model for 2024-T3 were calibrated using experimental data obtained from the literature [59]. The calibrated values are listed in Table 3.

### 3.4. Parameters in the improved pit evolution model

The pit evolution parameters in Eq. (22) can be classified as two different types: deterministic variables and random variables.

The deterministic variables are self-explanatory. These include  $M$ ,  $\rho$ ,  $n$ ,  $\Delta H$ , and  $T$ , the values of which are given in Table 4. The random variable  $I_{p0}$  usually obeys a Weibull distribution. In this study,

**Table 4**  
Calibrated parameter values for the pit evolution model.

Parameters	Values
$M$	2700 kg/mol
$\rho$	2700 kg/m <sup>3</sup>
$n$	3
$\Delta H$	40 kJ/mol
$T$	293 K
$I_{p0}$	0.0113A

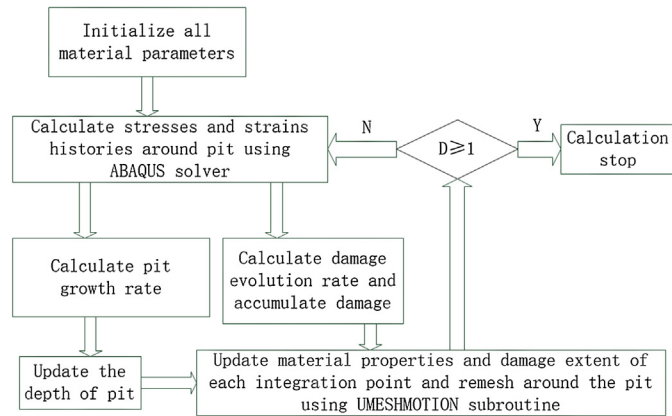


**Fig. 3.** Flowchart of the numerical algorithm in the corrosion fatigue case.

we used the mean value of  $I_{p0}$  to study the corrosion fatigue problem.  $I_{p0}$  represents the electrochemical process that influences the pit growth. The value of  $I_{p0}$  is calibrated by fitting the growth law expressed by Eq. (22) to pit depths measured at different times in corrosion fatigue experiments. The results of the corrosion fatigue experiment conducted by Ishihara et al. [23] were used to validate the improved pit evolution model presented in Section 2.3.2. A calibrated value of 0.0113C/s was obtained for  $I_{p0}$  by using a set of pit depth measurements obtained by Ishihara et al. [23]. The other set of pit depth measurements from that experiment were used to verify the model's prediction results. The calibration and verification processes are described in Section 6.2.

#### 4. Computational methodology

The theoretical models mentioned in Section 3 were implemented numerically by using the user subroutines UMAT and UMESHMOTION in ABAQUS [60]. For the case of the corrosion fatigue, the flowchart of the algorithm is shown in Fig. 3, and the detailed steps are presented below.

(1) The material parameters are initialized, and the initial damage is set to zero.

(2) The stresses and elastic and plastic strains around the pit are obtained by solving the coupled elasto-plastic damage constitutive equations, Eqs. (4)–(10). Because of the enormous amount of time required to simulate each loading cycle, the jump-in-cycle procedure was employed. This procedure assumes that in  $\Delta N$  cycles, the increment of fatigue damage for each cycle remains the same and the coupling effect between stress and damage is neglected for these  $\Delta N$  cycles. To obtain convergent results for the fatigue life, the value of  $\Delta N$  should satisfy the relationship  $\Delta N/\Delta N_i \approx 0.01$ –0.02. Further details are provided in the literature [44,57,61,62].

(3) The current pit depth and the fatigue damage evolution rates are calculated simultaneously.

a) The current pit depth is calculated based on Eq. (22), and the increment of pit depth in this block is thus obtained. The new shape of pit is formed by moving the surface nodes at the end of each increment. An advection equation based on the Lax-Wendroff method

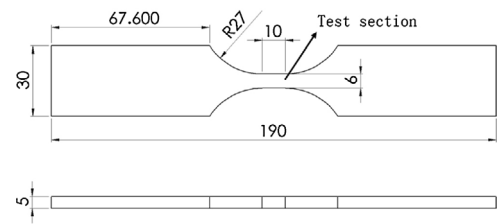


**Fig. 4.** Shape and dimensions of the test section of the specimen [23].

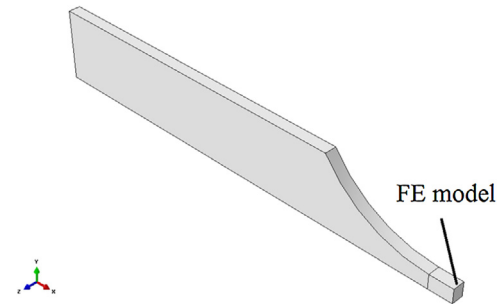


**Fig. 5.** 1/8 portion of the specimen in the literature [23] and the position of the FE model.

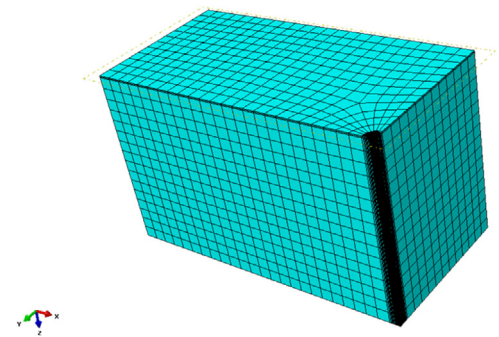


**Fig. 6.** FE model for verification of the improved pit evolution model.

[60], which is a second-order numerical method, is solved to remap the material variables into the new positions.

b) The fatigue damage evolution rates are calculated using Eqs. (13) and (17), based on the stresses and accumulated plastic strain histories. The larger of the two fatigue damage rates is assigned in the current block [56,57], i.e.,

$$\frac{dD}{dN} = \max \left\{ \frac{dD_e}{dN}, \frac{dD_p}{dN} \right\} \quad (29)$$

(4) At the end of the current block, all material parameter values and damage extent of each integration point will be updated.

(5) Steps (2)–(4) are repeated until the accumulated damage at any integration point reaches the critical value,  $D_c$ , which was set to 1 in this study.

#### 5. Finite element model

The FE model used to verify the improved pit evolution was established based on experiments conducted by Ishihara et al. [23]. The shape and dimensions of the specimen are illustrated in Fig. 4. A 1/8 portion of the specimen is shown in Fig. 5 and the FE model of the 1/8 portion of the test section is shown in Fig. 6. Symmetric boundary conditions were applied at three planes of symmetry. The pit depth calculated by the pit evolution model was compared with the experimental results reported in the literature. Two cases of

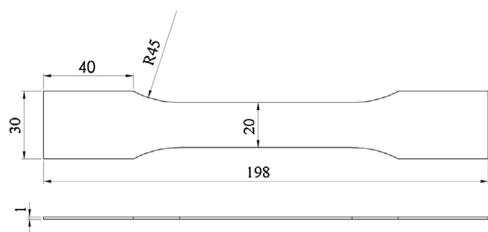


Fig. 7. Shape and dimensions of the specimen as reported in the literature [58].

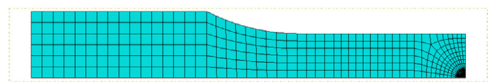


Fig. 8. Mesh of the FE model used for the corrosion fatigue case.

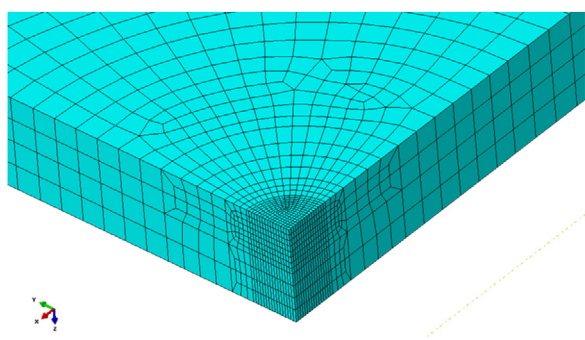


Fig. 9. Local mesh around the pit.

remote tension-compression fatigue loadings with the maximum tensile stresses of 50 MPa and 20 MPa were adopted in the calculation. The stress ratio  $R$  was  $-1$ , and the loading frequency was 10 Hz. The critical pit was positioned in the middle of the specimen surface, and the initial depth was set to zero. The element type, C3D8, was chosen for use in this study.

The geometry of the specimen tested for corrosion fatigue [58] is shown in Fig. 7. In this study, 1/8 portion of the specimen was modeled, and symmetric boundary conditions were applied at the three planes of symmetry. Remote tension-tension fatigue loadings with the maximum tensile stresses of 238 MPa and 190 MPa were applied on the specimen. The stress ratio  $R$  was 0.1, and the loading frequency was 1 Hz. The critical pit was positioned in the middle of the specimen surface, and the initial depth is set to zero. Fig. 8 illustrates the mesh of the FE model used in the corrosion fatigue model, and Fig. 9 illustrates the local mesh around the pit center. Fig. 10 illustrates the local mesh during the growth of the pit. The mesh density was determined to ensure both accuracy and efficiency of the calculation. The results of the stress convergence study required for implementation of the numerical calculation are presented in Section 6.1.

## 6. Results and discussion

### 6.1. Verification of stress convergence

It is relatively easy to obtain a convergence of the results for stress in a specimen without a pit because the stress is uniform along the cross section. However, the mesh around the critical pit must be very fine to obtain accurate stress results when a pit appears and grows.

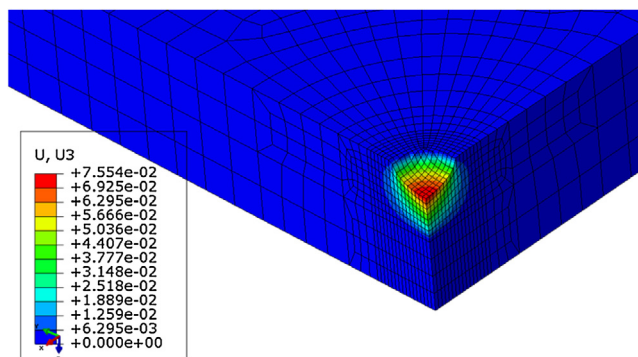


Fig. 10. Local mesh during the growth of the pit.

Table 5

Number of elements around the pit and the maximum stresses for three mesh densities.

Mesh density	Coarse	Medium	Fine
Number of elements around pit	270	1719	4344
Maximum stress	328.3	332.1	333.4
Relative error		1.16%	0.39%

To select a suitable mesh density, we reconstructed the geometric model based on the pit shape obtained from a particular step of the UMESHMOTION calculation. The new geometric model with a specific pit size was then remeshed, and the mesh density was gradually increased to achieve convergence in the stress calculations. After this, the suitable mesh density was used for the UMESHMOTION calculations.

Fig. 11(a)–(c) illustrate the stress contours of the coarse mesh, medium density mesh, and fine mesh, respectively. The high stress area was the focus of this fatigue research. The stress distribution along the path marked in Fig. 11 with red points was selected for comparison of the results for the three mesh densities. Table 5 shows the number of elements around the pits, the maximum stresses, and the relative errors for the three mesh densities. A comparison of the stress results is presented in Fig. 12 which shows that the stress results corresponding to the medium density mesh are the most satisfactory. Therefore, this mesh density was selected for the UMESHMOTION calculations.

### 6.2. Verification of improved pit evolution model

The applicability of the improved pit evolution model described in Section 2.3 was verified as described in this section. One set of experimental data on pit depth obtained by Ishihara et al. [23] was used to determine the parameter values, and the other set was used to verify the prediction results.

The corrosion solvent used in Ishihara's experiment [23] was a 3% NaCl solution with pure water. It should be noted that in Ishihara's experiment [23], the experimental data for the pit depth were obtained by separating the observation area into nine small areas, and the maximum pit depth for each of the nine areas was measured. Given the sensitivity of the measurements to the individual characteristics of a particular corrosion pit, the variation of the distribution of the maximum pit depth,  $F(a)$ , which is used to determine the general characteristics of pit growth behavior, was investigated. Table 6 illustrates the scope of the maximum pit depth at the maximum stress of 50 MPa. These values were obtained from the literature [23]. Based on the range of measured pit depths at the corrosion time of 0.5 h, a rough value of  $I_{p0}$  was estimated to be 0.0113C/s to simulate the process of the corrosion fatigue in the experiment conducted by Ishihara.

**Table 6**  
Distribution of pit depth at stress amplitude of 50 MPa and  $f = 10$  Hz for various corrosion times [23].

Corrosion time, h	0.5	1	2	5	10
Pit depth distribution obtained from experimental results, $\mu\text{m}$	3–5	4–6	4–8	7–10	8–12

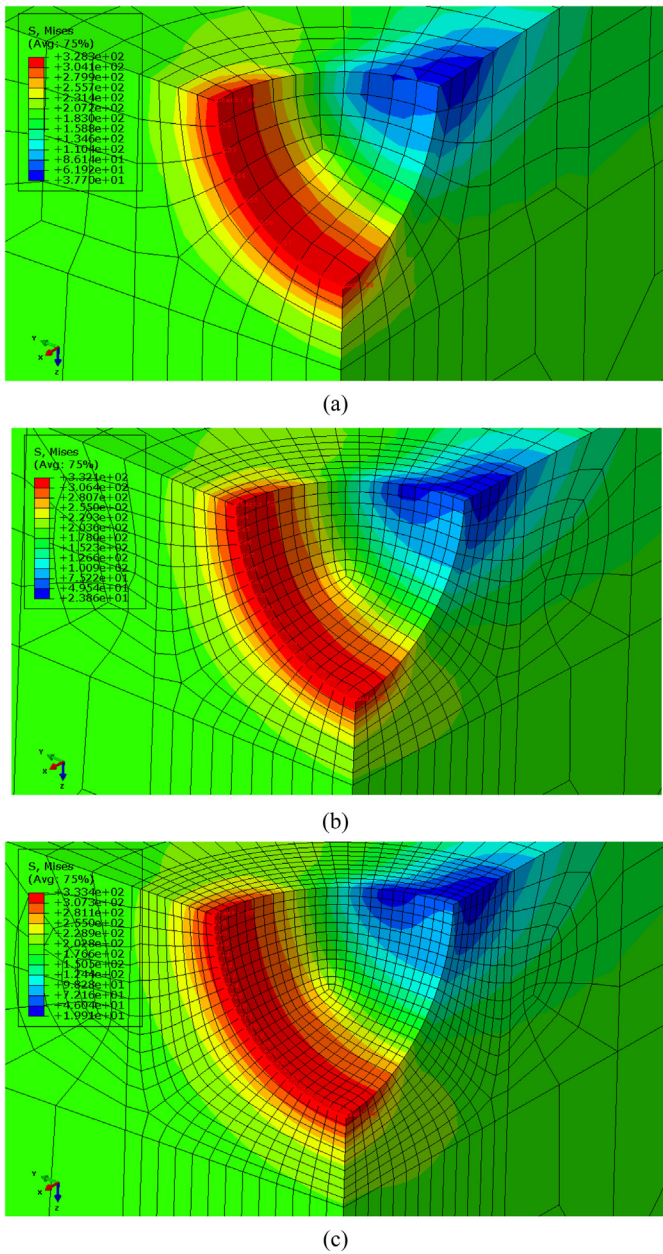


**Fig. 11.** Convergence of stresses around the pit: (a) stress contours of coarse mesh, (b) stress contours of middle density mesh, (c) stress contours of fine mesh.

The elliptical ratio,  $\lambda$ , influences the stress concentration factor. A considerable difference can be found between the hemispherical and semi-ellipsoidal pit growth. Thus, assumption of a suitable value of  $\lambda$  is crucial to accurately simulating the process of corrosion fatigue. Burns and Kim [21,22] proposed several hypotheses based on their experimental observations. According to their observations of fracture surface, they found that the shape factors,  $c/a$ , of a semi-elliptical pit cluster adjacent to a dominant crack were 2 and 1.92, while those of the first distinctive semi-elliptical crack were 1.54 and 1.56 [21].

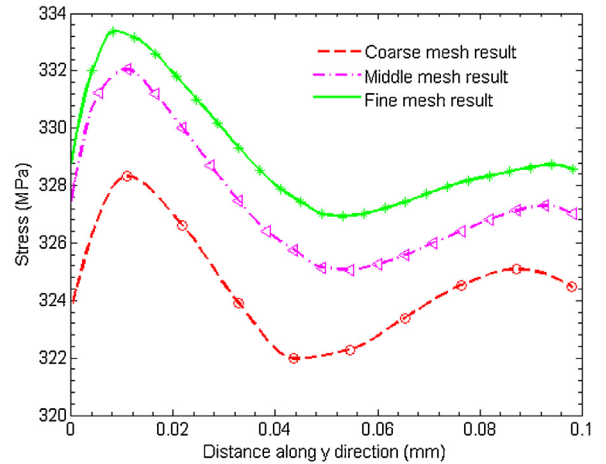


**Fig. 12.** Comparative results of coarse mesh and refined mesh along the pit surface path.

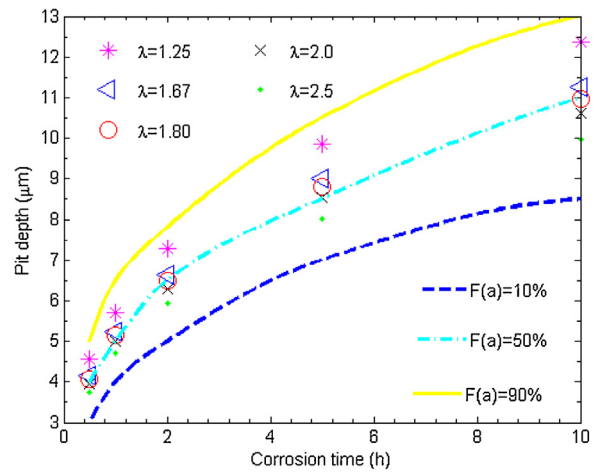


**Fig. 13.** Calculated pit depth versus corrosion time for various values of  $\lambda$  (the distribution of  $F(a)$  was obtained from experimental data in the literature [23]).

Calculated values of pit depth versus time for different values of  $\lambda$  are shown in Fig. 13. The three curves in Fig. 13 represent the experimental pit depth versus time for different values of the probability,  $F(a)$ . These values were obtained from the literature [23]. As Fig. 13 shows, the calculated values corresponding to the cases of  $\lambda = 1.8$  and 2 agree well with the experimental curve for a probability of 50%. Thus, shape factors of  $\lambda = 1.8$  and 2 were selected for later calculations. These values are consistent with experimental observations reported by Burns and Kim et al. [21,22].

To verify the applicability of the values of  $I_{p0}$  and  $\lambda$ , pit depths at different corrosion fatigue times for a maximum stress of 20 MPa were calculated. Table 7 shows the predicted and measured pit depths. As the table shows, the predicted pit depths agree well with the experimental data for the probability of 50%. Therefore, the improved pit evolution model was concluded to accurately predict pit growth.

Fig. 14 illustrates the pit geometry and the von Mises stress contours around the pit for a stress amplitude of 50 MPa and a shape factor  $\lambda = 2$  for corrosion times of 5 and 10 h.

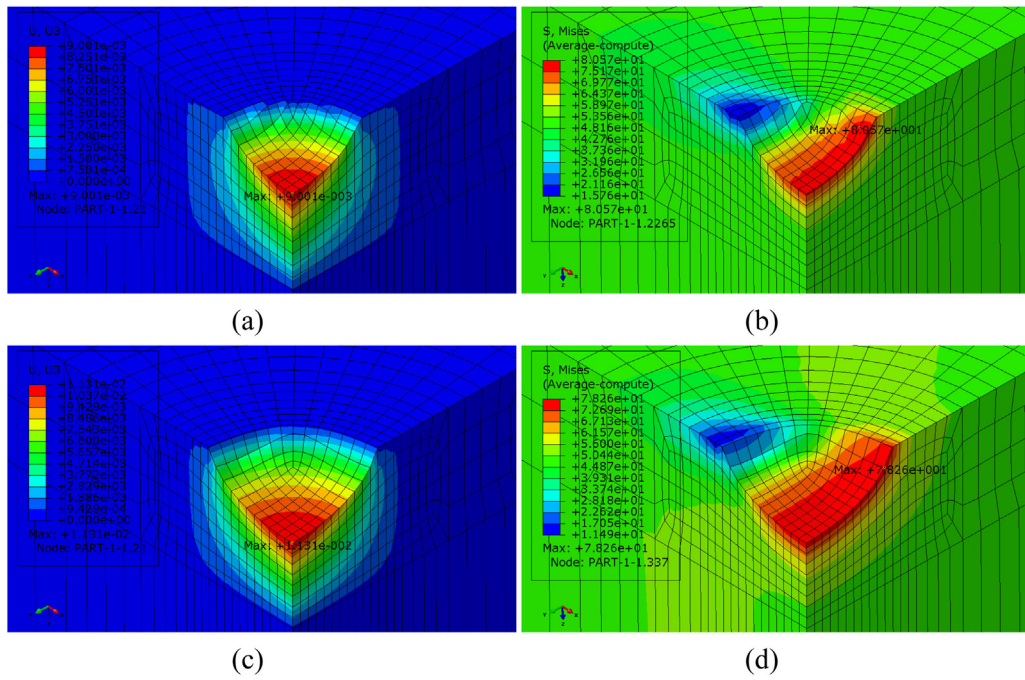


Fig. 14. Contours of pit geometry and stress under a stress amplitude of 50 MPa and  $f = 10$  Hz: (a) and (b) at  $t = 5$  h, (c) and (d) at  $t = 10$  h.

Table 7

Comparative results of the distribution of pit depth at a stress amplitude of 20 MPa and  $f = 10$  Hz (the distribution of  $F(a)$  was obtained from experimental data in the literature [23]).

Corrosion time, (h)	2	5	10
Pit depth calculated for $\lambda = 1.8 \mu\text{m}$	3.34	4.54	5.73
Pit depth calculated for $\lambda = 2 \mu\text{m}$	3.31	4.5	5.69
Pit depth when the distribution $F(a) = 50\%$ , $\mu\text{m}$	4.5	5	6

6.3. Numerical calculation of corrosion fatigue

The verification case mentioned above was used to verify the improved pit evolution model. The stress level was relatively low in this case, which resulted in a very long fatigue life. Thus, the corrosion fatigue life was not investigated. The results of the corrosion fatigue experiment conducted by Kong [58] were used to validate the corrosion fatigue model and examine the complex interaction between corrosion and fatigue. The geometry of the specimen for the test was described in Section 5. The corrosion solvent used in Kong’s experiment [58] was 5% NaCl solution ( $\text{pH} = 4$ ). The following sections describe the numerical conducted and the mechanisms and factors involved in corrosion fatigue.

6.3.1. Evolution of corrosion pit

The case of a specimen undergoing cyclic loading at a maximum stress of 190 MPa was considered to illustrate the evolution of corrosion pit. The location of the critical pit is shown in Fig. 15. Because of the lack of experimental data from Kong’s experiment, an  $I_{p0}$  value of  $0.0352C/s$  was used based on a calibration by Hallow and Wei [19]. The corrosion solvent in Hallow and Wei’s experiment was 5% NaCl solution ( $\text{pH} \approx 6$ ), which was almost the same with Kong’s experiment. A comparison between the calculated results and experimental data suggests that this value of  $I_{p0}$  was appropriate.

Fig. 16 shows the pit geometry evolution along the specific path in the cross section perpendicular to the loading direction, which is

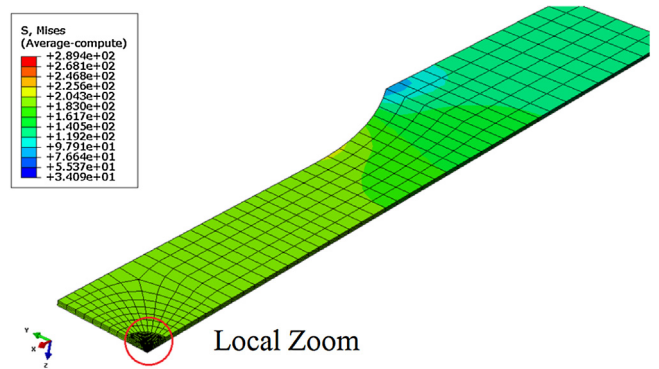


Fig. 15. Stress contours of the 1/8 specimen when crack initiates at a maximum stress of 190 MPa.

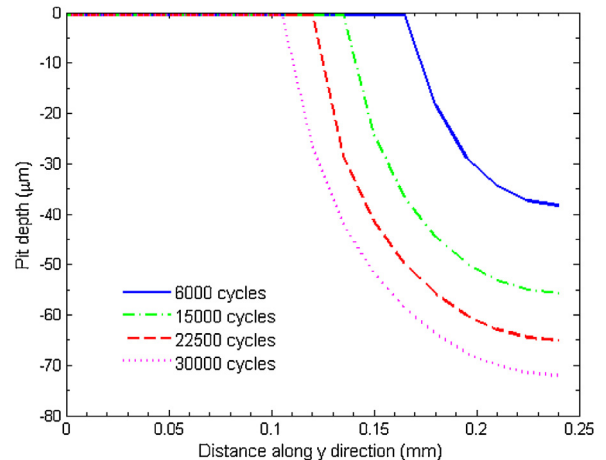


Fig. 16. Evolution of pit geometry at the cross section perpendicular to the loading direction.

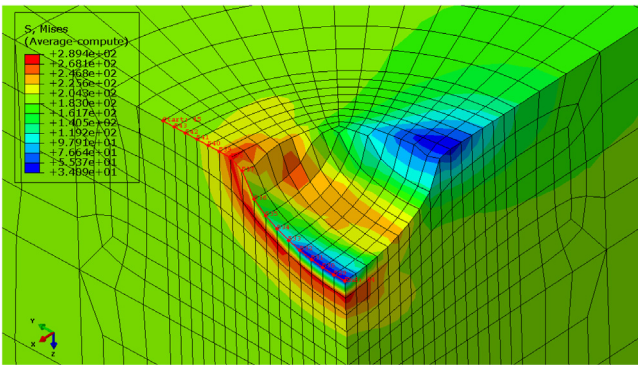


Fig. 17. Stress contours when crack initiates at a maximum stress of 190 MPa and  $\lambda = 1.8$ .

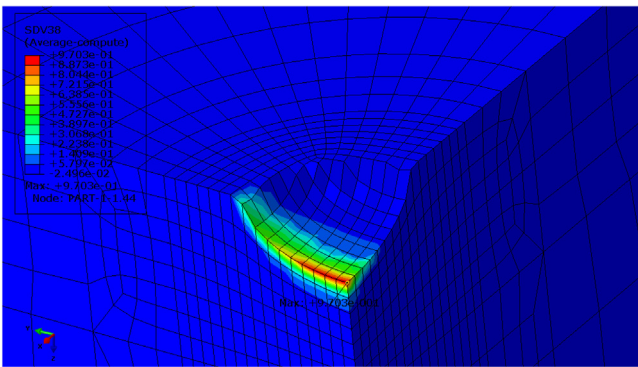


Fig. 18. Damage contours when crack initiates at a maximum stress of 190 MPa and  $\lambda = 1.8$ .

marked in Fig. 17 with red points. As shown in Fig. 16, the pit grows as the number of fatigue loading cycles increases. The growth is initially rapid and then slows down.

The occurrence of a pit affects the stress concentration, and fatigue damage accumulates rapidly in the high stress area. Less fatigue damage occurs away from the pit. However, the fatigue damage is much larger at the center of the pit because the stress concentration occurs first at this position. Therefore, the accumulated fatigue damage is larger, which makes the evolution rate faster at the center of the pit than in other areas.

Figs. 17 and 18 show the von Mises stress contours and damage contours respectively, when a crack initiates. These figures show that fatigue damage accumulates at the surface of the pit. The mechanical properties of the surface material degrade with the increase of the number of cycles, which makes the stresses at the surface of the pit much smaller than those on the subsurface. The maximum stress occurs on the subsurface of the pit when a crack initiates at the root of the pit surface.

### 6.3.2. Interaction between corrosion and fatigue damage

The corrosion fatigue process can be divided into two stages. The growth of corrosion pit plays a major role at the early stage. Stress concentration is not very severe when the corrosion pit is relatively small and the plastic and elastic fatigue damages are negligible. Figs. 19 and 20 illustrate the distributions of the von Mises stress along the path marked in Fig. 17 with red points at different numbers of cycles. That path is at the cross section perpendicular to the loading direction. As Fig. 19 shows, the high stress area gradually expands with the increase of the number of cycles because the pit grows larger and larger. At the same time, stresses in the high stress area decrease slowly as the fatigue damage accumulates at the bottom of the pit.

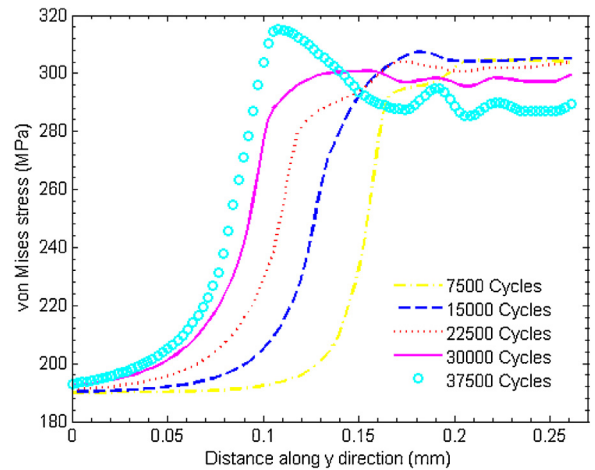


Fig. 19. Distribution of the von Mises stress along y direction at different number of cycles at the early stage.

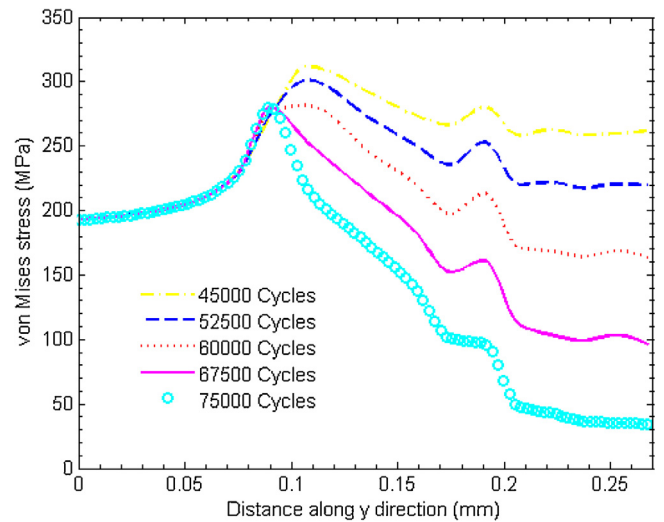


Fig. 20. Distribution of the von Mises stress along y direction at different number of cycles at the later stage.

In the later period of corrosion fatigue, the accumulation of fatigue damage is dominant. The result is that the stresses in the high stress area decrease more rapidly after 30,000 load cycles are applied. Then the position of the maximum stress gradually moves to the edge of the pit. This occurs because the stresses in the pit bottom area gradually decrease with fatigue damage accumulation. The stresses around the pit redistribute, and the fatigue damage at the edge of the pit is relatively small compared to that at the bottom. As illustrated in Figs. 17 and 18, the mechanical properties of material on the surface of the pit degrade with fatigue damage accumulation. Fig. 20 illustrates the degradation trend of the material at the pit surface. As the number of cycles increases, stresses in the high stress area gradually decrease. Closer to the center of the corrosion pit, the stresses decrease more dramatically. Eventually, a crack initiates at the location at which the stress decreases the most.

During the process of corrosion fatigue, pit evolution and fatigue damage evolution interact with each other. On one hand, the pit evolution rate is related to the stress state at the center of the pit. The stress at the center of the pit changes as the fatigue damage develops. On the other hand, the growth of the pit influences the stress state of the material around the pit. Therefore, the interaction

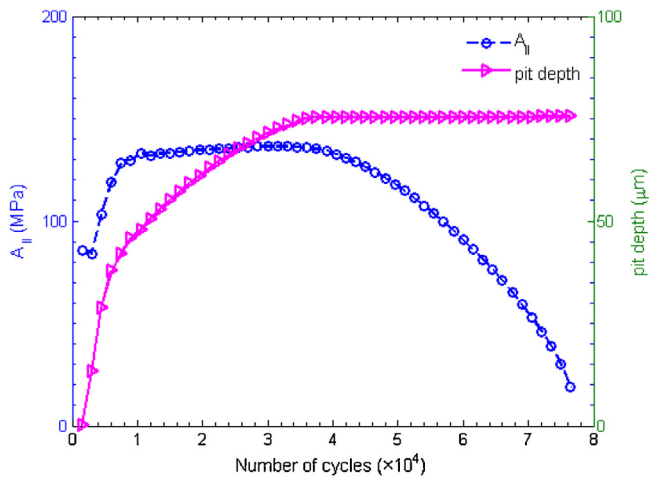


Fig. 21. Evolution of pit depth and amplitude of the octahedral shear stress,  $A_{II}$ , at a maximum stress of 190 MPa.

between the pit growth and fatigue damage evolution is brought about by the variation in the stress field.

To illustrate the variation in the stress field during the processes of pit evolution and fatigue damage evolution, the amplitude of the octahedral shear stress at the center of pit,  $A_{II}$ , and the pit depth are plotted against the number of cycles in Fig. 21. The plots show that  $A_{II}$  initially increases as the number of fatigue loading cycles increases, and then decreases after a period of almost no change. The increasing trend at the beginning is due to the fact that the pit growth increases the effect of the stress concentration. As the pit grows, the stress concentration becomes more and more severe. Although fatigue damage accumulates at the same time, the effect of pit growth is more significant than the effect of fatigue damage in this stage.

However, the pit grows slowly and even stops growing at the later stage. The fatigue damage becomes severe and increases rapidly. Thus, the effect of fatigue damage becomes more noticeable. At this point, the value of  $A_{II}$  starts to decrease, and the pit grows more slowly. The pit stops growing completely when  $A_{II}$  decreases to a particularly small value. The trend illustrated in Fig. 21 is consistent with the observations from corrosion fatigue experiments [29]. In which the authors noted that as the corrosion product accumulated in the pits, the new regions of pits is protected from being corroded. The effect of corrosion damage on the whole corrosion fatigue process is gradually reduced. It is worth noting that the model proposed in this study is just one of many possible models that can describe pit growth and that its physical and chemical mechanisms still require further study. Fig. 22 shows the evolution of fatigue damage at the center of the pit.

It should be noted that the pit depth may decrease according to Eq. (22) when  $A_{II}$  decreases to a sufficiently small value. However, this is not realistic from a physical point of view. Thus, the pit shape is set to be constant in this situation.

### 6.3.3. Plastic damage accumulation during corrosion fatigue

Two damage models corresponding to the calculations of elastic and plastic damage were adopted in this study. To evaluate the effect of plastic damage accumulation during corrosion fatigue, two loading conditions, i.e., a lower loading with a maximum stress of 190 MPa and a higher loading with a maximum stress of 238 MPa, were considered. For the case of the lower loading, the elastic damage evolution and the plastic damage evolution are shown in Fig. 23. As the figure shows, the elastic damage evolution rate increases monotonically. The plastic damage evolution rate is much smaller than the elastic damage evolution rate throughout almost the entire

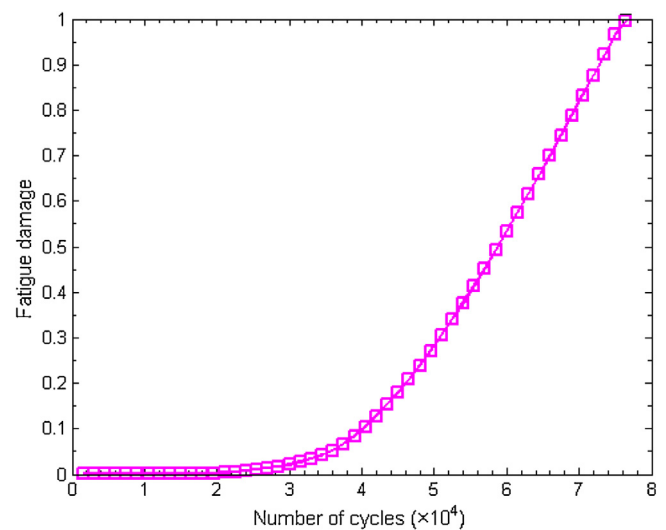


Fig. 22. Evolution of fatigue damage at a maximum stress of 190 MPa.

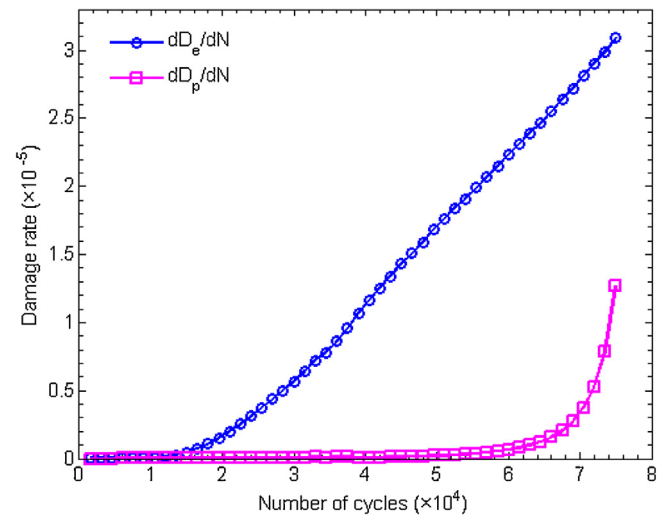


Fig. 23. Evolution of two fatigue damage rates at a maximum stress of 190 MPa.

process except at the beginning stage when they are both very small. This means that the plastic damage can be neglected for this case.

Fig. 24 shows the case of the higher loading. The elastic damage evolution rate increases at the beginning stage, then becomes nearly constant, and then drops down at the end stage. The plastic damage evolution rate is also small in the beginning. However, it increases dramatically at the end stage and becomes larger than the elastic damage evolution rate. Thus, plastic damage must be considered for the case of higher loading.

### 6.3.4. Influence of pit morphology on predicted lives

As discussed in the introduction, the pit shape influences the stress concentration factor around the pit. The shape factor,  $\lambda$ , also affects the pit evolution. This section describes an investigation of the effect of  $\lambda$  on the fatigue crack initiation life. Five different values of  $\lambda$  were used to simulate the process of corrosion fatigue. Tables 8 and 9 show the comparative results between the predicted lives and the experimental results under the loading with maximum stresses of 190 MPa and 238 MPa, respectively. Five sets of experimental fatigue lives were obtained from the literature [58]. The result shows that an increase in the ratio,  $\lambda$ , leads to an increase in the corrosion fatigue life. From a qualitative point of view, this

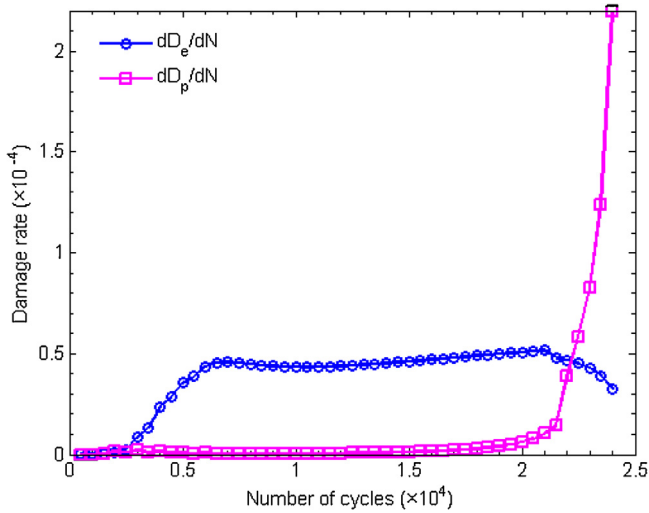


Fig. 24. Evolution of two fatigue damage rates at a maximum stress of 238 MPa.

Table 8 Predicted lives for various values of  $\lambda$  for a maximum stress of 190 MPa and experimental data [58].

Experiments	Experimental life, (cycles)	Mean life (cycles)
	84,313; 85,150; 55,129; 69,455; 85,512	74,858
Theoretical model	$\lambda = c/a$	Predicted life
	1	30,000
	1.25	41,250
	1.667	70,500
	1.8	76,500
	2	102,000

Table 9 Predicted lives for various values of  $\lambda$  for maximum stress of 238 MPa and experimental data [58].

Experiments	Experimental life (cycles)	Mean life (cycles)
	35,266; 31,637; 39,682; 37,530; 56,153	39,263
Theoretical model	$\lambda = c/a$	Predicted life
	1	700
	1.25	10,600
	1.667	20,400
	1.8	24,000
	2	33,000

is because the stress concentration of the semi-ellipsoidal pits is small and becomes smaller as  $\lambda$  increases. For the case of loading with a maximum stress of 190 MPa, the predicted life when  $\lambda = 1.8$  is in good agreement with the experimental results. Furthermore, for the case of loading with a maximum stress of 238 MPa, the predicted life when  $\lambda = 2$  agrees well with the experimental life. Therefore, it can be concluded that the values of  $\lambda$  in the range of 1.8–2 are applicable to the simulation of the corrosion fatigue of aluminum alloy 2024-T3.

6.3.5. Effect of stress level on critical pit depth

The results in Table 9 show that when the hemispherical assumption is adopted, crack initiation from the pit site can occur extremely rapidly at a high stress level even when the pit depth is relatively small. Table 10 shows the effect of stress level on the critical pit depth for various values of  $\lambda$ . The critical pit depth decreases as the stress level increases, which implies that fatigue crack can initiate from very shallow pits at a high stress. This is because a high stress can cause a plastic strain around even a very shallow pit. Plastic strain accelerates the fatigue damage accumulation and

Table 10 Effect of stress level on the critical pit depth.

$\lambda = c/a$	Critical pit depth at different stress level ( $\mu\text{m}$ )	
	190 MPa	238 MPa
1.8	75.5	61.8
2	87.4	66.7

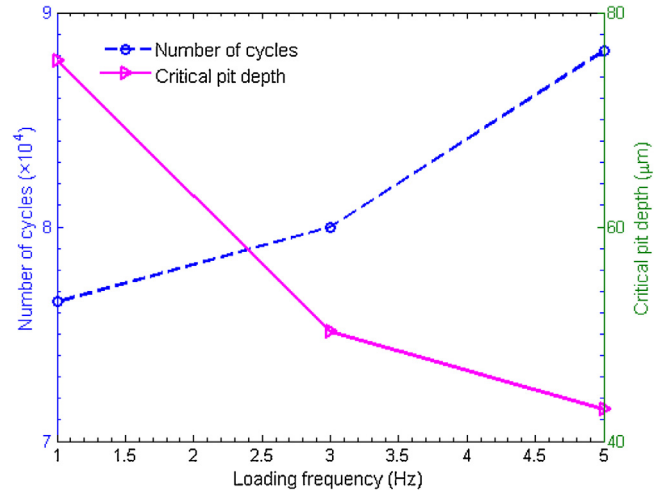


Fig. 25. Influence of loading frequency on fatigue lives and critical pit depth.

induces the crack initiation at a less number of cycles. Therefore, the critical pit depth becomes smaller when the stress level is higher.

6.3.6. Influence of fatigue loading frequency

As Eq. (20) shows, the pit depth increases with the increase of corrosion time. A higher loading frequency corresponds to a reduction in the corrosion time for a given number of loading cycles. The effect of corrosion is then relatively weakened, and fatigue damage plays a more important role in the process of corrosion fatigue. Thus, the predicted lives increase with the increase of loading frequency, as shown in Fig. 25. In addition, the critical pit depth decreases with the increase of loading frequency.

7. Conclusions

A continuum damage mechanics approach combined with an improved pit evolution model was presented in this paper to study the corrosion fatigue of aluminum alloy 2024-T3. The following key findings were obtained:

- (1) The improved pit evolution model can describe the growth of the corrosion pit under multiaxial cyclic stresses. It was convenient to simulate the evolution of corrosion pit by means of a subroutine termed UMESHMOTION in ABAQUS. The calculated results agreed well with the experimental data.
- (2) The corrosion fatigue life of aluminum 2024-T3 was calculated by taking into account the coupling effect between the pit growth and the fatigue damage evolution via a user subroutine in ABAQUS. The predicted lives agreed well with the experimental results.
- (3) There is an evident interaction between the pit growth and fatigue damage evolution. The growth of the corrosion pits gives rise to stress concentrations, and the cyclic stress in turn accelerates the growth of the pits. At the same time, the accumulated fatigue damage degrades the mechanical properties of the material around a pit and results in the redistribution of stresses around the pit, which in turn influences the pit growth process.

- (4) A high stress level significantly decreases the corrosion fatigue lives. At a high stress level, crack can initiate from a shallow pit, and the plastic fatigue damage is much larger in the later phase of corrosion fatigue.
- (5) With the increase of loading frequency, the corrosion time decreases for the same number of cycles. Thus the effect of corrosion is weakened and the fatigue life is accordingly extended.

## Acknowledgment

Authors are grateful to George Z Voyiadjis (Boyd Professor of Louisiana State University) for his careful reading and giving valuable suggestions on improving the quality of the manuscript.

## References

- [1] J. Rajasanka, Nagesh R. Iyer, A probability-based model for growth of corrosion pits in aluminium alloys, *Eng. Fract. Mech.* 73 (2006) 553–570.
- [2] E.J. Dolley, B. Lee, R.P. Wei, The effect of pitting corrosion on fatigue life, *Fatigue Fract. Eng. Mater. Struct.* 23 (2000) 555–560.
- [3] R.P. Wei, C.M. Liao, M. Gao, A transmission electron microscopy study of constituent-particle-induced corrosion in 7075-T6 and 2024-T3 aluminum alloys, *Metall. Mater. Trans. A* 29 (1998) 1153–1160.
- [4] P.S. Pao, S.J. Gill, C.R. Feng, On fatigue crack initiation from corrosion pits in 7075-T7351 aluminum alloy, *Scripta Mater.* 43 (2000) 391–396.
- [5] Q.Y. Wang, R.M. Pidaparti, M.J. Palakal, Comparative study of corrosion-fatigue in aircraft materials, *AIAA J.* 39 (2001) 325–330.
- [6] V. Guillaumin, G. Mankowski, Localized corrosion of 2024 T351 aluminium alloy in chloride media, *Corros. Sci.* 41 (1998) 421–438.
- [7] A. Boag, A.E. Hughes, A.M. Glenn, T.H. Muster, D. McCulloch, Corrosion of AA2024-T3 part I: localised corrosion of isolated IM particles, *Corros. Sci.* 53 (2001) 17–26.
- [8] N. Birbilis, M.K. Cavanaugh, R.G. Buchheit, Electrochemical behavior and localized corrosion associated with Al7Cu2Fe particles in aluminum alloy 7075-T651, *Corros. Sci.* 48 (2006) 4202–4215.
- [9] K. Jones, D.W. Hoepfner, Pit-to-crack transition in pre-corroded 7075-T6 aluminum alloy under cyclic loading, *Corros. Sci.* 47 (2005) 2185–2198.
- [10] K.K. Sankaran, R. Perez, K.V. Jata, Effects of pitting corrosion on the fatigue behavior of aluminum alloy 7075-T6: Modeling and experimental studies, *Mater. Sci. Eng. A* 297 (2001) 223–229.
- [11] C.L. Harmsworth, Effect of corrosion on the fatigue behavior of 2024-T4 aluminum alloy, *ASD Tech. Rep.* 61–121 (1961) 1–7.
- [12] K. Jones, D.W. Hoepfner, Prior corrosion and fatigue of 2024-T3 aluminum alloy, *Corros. Sci.* 48 (2006) 3109–3122.
- [13] R. Ebara, Corrosion fatigue crack initiation in 12% chromium stainless steel, *Mater. Sci. Eng. A* 468 (2007) 109–113.
- [14] Y. Kondo, Prediction of fatigue crack initiation life based on pit growth, *Corrosion* 45 (1989) 7–11.
- [15] D.G. Harlow, R.P. Wei, Probability approach for prediction of corrosion and corrosion fatigue life, *AIAA J.* 32 (1994) 2073–2079.
- [16] E. Ghali, W. Dietzel, K.U. Kainer, Testing of general and localized corrosion of magnesium alloys: a critical review, *J. Mater. Eng. Perform.* 13 (2004) 517–529.
- [17] E.N. Codaro, R.Z. Nakazato, A.L. Horovistiz, L.M.F. Ribeiro, R.B. Ribeiro, L.R.O. Hein, An image processing method for morphology characterization and pitting corrosion evaluation, *Mater. Sci. Eng. A* 334 (2002) 298–306.
- [18] H.P. Godard, The corrosion behavior of aluminum in natural waters, *Can. J. Chem. Eng.* 38 (2011) 167–173.
- [19] D.G. Harlow, R.P. Wei, Probabilities of occurrence and detection of damage in airframe materials, *Fatigue Fract. Eng. Mater. Struct.* 22 (2001) 427–436.
- [20] G.S. Chen, K.-C. Wan, M. Gao, R.P. Wei, T.H. Flournoy, Transition from pitting to fatigue crack growth—modeling of corrosion fatigue crack nucleation in a 2024-T3 aluminum alloy, *Mater. Sci. Eng. A* 219 (1996) 126–132.
- [21] S. Kim, J.T. Burns, R.P. Gangloff, Fatigue crack formation and growth from localized corrosion in Al–Zn–Mg–Cu, *Eng. Fract. Mech.* 76 (2009) 651–667.
- [22] J.T. Burns, S. Kim, R.P. Gangloff, Effect of corrosion severity on fatigue evolution in Al–Zn–Mg–Cu, *Corros. Sci.* 52 (2010) 498–508.
- [23] S. Ishihara, S. Saka, Z.Y. Nan, T. Goshima, S. Sunada, Prediction of corrosion fatigue lives of aluminium alloy on the basis of corrosion pit growth law, *Fatigue Fract. Eng. Mater. Struct.* 29 (2006) 472–480.
- [24] A. Turnbull, L.N. McCartney, S. Zhou, A model to predict the evolution of pitting corrosion and the pit-to-crack transition incorporating statistically distributed input parameters, *Corros. Sci.* 48 (2006) 2084–2105.
- [25] M. Amiri, A. Arcari, L. Airolidi, M. Naderi, N. Iyyer, A continuum damage mechanics model for pit-to-crack transition in AA2024-T3, *Corros. Sci.* 98 (2015) 678–687.
- [26] D.W. Hoepfner, in: J.T. Fong (Ed.), *Fatigue Mechanisms*, STP 675, ASTM Philadelphia, PA, 1979, p. p841.
- [27] M. Muller, *Metall. Trans.* 19 (13,4) (1982) 649.
- [28] Y.C. Xiao, S. Li, Z. Gao, A continuum damage mechanics model for high cycle fatigue, *Int. J. Fatigue* 20 (1998) 503–508.
- [29] W.P. Hu, Q.A. Shen, M. Zhang, Q.C. Meng, X. Zhang, Corrosion-fatigue life prediction for 2024-T62 aluminum alloy using damage mechanics-based approach, *Int. J. Damage Mech.* 21 (2012) 1245–1266.
- [30] S. Sarkar, J.E. Warner, W. Aquino, A numerical framework for the modeling of corrosive dissolution, *Corros. Sci.* 65 (2012) 502–511.
- [31] N. Kota, S.M. Qidwai, A.C. Lewis, V.G. DeGiorgi, Microstructure-based numerical modeling of pitting corrosion in 316 stainless steel, *ECS Trans.* 50 (31) (2013) 155–164.
- [32] W. Sun, L.D. Wang, T.T. Wu, G.C. Liu, An arbitrary Lagrangian–Eulerian model for modelling the time-dependent evolution of crevice corrosion, *Corros. Sci.* 78 (2014) 233–243.
- [33] J. Lemaitre, J.L. Chaboche, A.K. Maji, *Mechanics of Solid Materials*, Cambridge University Press, 1990.
- [34] J. Lemaitre, R. Desmorat, *Engineering Damage Mechanics*, Springer, 2006.
- [35] C.L. Chow, J. Wang, An anisotropic theory of continuum damage mechanics for ductile fracture, *Eng. Fract. Mech.* 27 (1987) 547–558.
- [36] G.Z. Voyiadjis, P.I. Kattan, 2006. A coupled anisotropic damage model for the inelastic response of composite materials – *Adv. Damage Mech. (Second Edition) – Chapter 17*, *Adv. Damage Mech.* 183 479–542.
- [37] L.L. Sun, W.P. Hu, M. Zhang, Q.C. Meng, An anisotropic damage model based on microstructure of boom-panel for the fatigue life prediction of structural components, *Fatigue Fract. Eng. Mater. Struct.* 37 (2014) 1186–1196.
- [38] J. Lemaitre, *A Course on Damage Mechanics*, Springer Science & Business Media, 2012.
- [39] J.L. Chaboche, Time-independent constitutive theories for cyclic plasticity, *Int. J. Plast.* 2 (1986) 149–188.
- [40] J.L. Chaboche, A review of some plasticity and viscoplasticity constitutive theories, *Int. J. Plast.* 24 (2008) 1642–1693.
- [41] P.I. Kattan, G.Z. Voyiadjis, A coupled theory of damage mechanics and finite strain elasto-plasticity—I. Damage and elastic deformations, *Int. J. Eng. Sci.* 5 (1990) 421–435.
- [42] G.Z. Voyiadjis, P.I. Kattan, A coupled theory of damage mechanics and finite strain elasto-plasticity—II. Damage and finite strain plasticity, *Int. J. Eng. Sci.* 6 (1990) 505–524.
- [43] M. Chaudonneret, A simple and efficient multiaxial fatigue damage model for engineering applications of macro-crack initiation, *J. Eng. Mater. Technol.* 115 (1993) 373–379.
- [44] T. Zhang, P.E. Mchugh, S.B. Leen, Finite element implementation of multiaxial continuum damage mechanics for plain and fretting fatigue, *Int. J. Fatigue* 44 (2012) 260–272.
- [45] Y. Wang, G. Cheng, Y. Li, Observation of the pitting corrosion and uniform corrosion for X80 steel using in-situ and 3-D measuring microscope, *Corros. Sci.* (2016) 417–508.
- [46] G.T. Burstein, P.C. Pistorius, S.P. Mattin, The nucleation and growth of corrosion pits on stainless steel, *Corros. Sci.* 35 (1993) 57–62.
- [47] G.T. Burstein, C. Liu, Nucleation of corrosion pits in Ringer's solution containing bovine serum, *Corros. Sci.* 49 (2007) 4296–4306.
- [48] A. Trueman, Determining the probability of stable pit initiation on aluminium alloys using potentiostatic electrochemical measurements, *Corros. Sci.* 47 (2005) 2240–2256.
- [49] J. Kang, R.D. Fu, G.H. Luan, C.L. Dong, M. He, In-situ investigation on the pitting corrosion behavior of friction stir welded joint of AA2024-T3 aluminium alloy, *Corros. Sci.* 52 (2010) 620–626.
- [50] N. Murer, R.G. Buchheit, Stochastic modeling of pitting corrosion in aluminum alloys, *Corros. Sci.* 69 (2013) 139–148.
- [51] Z. Szklarska-Smialowska, Pitting corrosion of aluminum, *Corros. Sci.* 41 (1999) 1743–1767.
- [52] Proceeding Symposium Critical Factors in Localized Corrosion, 92–9, in: D.E. Williams, J. Stewart, P.H. Balkwill, G.S. Frankel, R.C. Newman (Eds.), *The Electrochem. Soc., Pennington, NJ*, 2016, p. 36.
- [53] D.G. Harlow, R.P. Wei, A probability model for the growth of corrosion pits in aluminum alloys induced by constituent particles, *Eng. Fract. Mech.* 59 (1998) 305–325.
- [54] M.R. Sriraman, R.M. Pidaparti, Life prediction of aircraft aluminum subjected to pitting corrosion under fatigue conditions, *J. Aircr.* 46 (2009) 1253–1259.
- [55] R.P. Wei, D.G. Harlow, Mechanistically based probability modeling, life prediction and reliability assessment, *Modell. Simul. Mater. Sci. Eng.* 13 (2005) R33–R51.
- [56] F. Shen, G.Z. Voyiadjis, W.P. Hu, Q.C. Meng, Analysis on the fatigue damage evolution of notched specimens with consideration of cyclic plasticity, *Fatigue Fract. Eng. Mater. Struct.* 38 (2015) 1194–1208.
- [57] F. Shen, W.P. Hu, G.Z. Voyiadjis, Q.C. Meng, Effects of fatigue damage and wear on fretting fatigue under partial slip condition, *Wear* 338–339 (2015) 394–405.
- [58] G.M. Kong, X.X. Gao, X.D. Li, Z.T. Mu, H. Lv, Damage mechanics based on model of LY12CZ aluminium alloy uniaxial corrosion-fatigue life prediction, *New Technol. New Process* (2) (2015) 78–81 (In Chinese).
- [59] X.R. Wu, *Handbook of Mechanics Properties of Aircraft Structure Metals*, Aviation Industry Press, 1997.
- [60] Karlsson Hibbett, *ABAQUS/standard: User's Sorensen Manual*, Karlsson Hibbett & Sorensen, 1998.
- [61] Z.X. Zhan, W.P. Hu, M. Zhang, Q.C. Meng, The fatigue life prediction for structure with surface scratch considering cutting residual stress, initial plasticity damage and fatigue damage, *Int. J. Fatigue* 74 (2015) 173–182.
- [62] Z.X. Zhan, W.P. Hu, Q.C. Meng, S.D. Shi, Continuum damage mechanics-based approach to the fatigue life prediction for aluminum alloy with impact pit, *Int. J. Damage Mech.* (2015) 7050–7451.